

Dark Matter in Dwarf Spheroidals I: Models

M.I. Wilkinson¹, J. Kley¹, N.W. Evans², G. Gilmore¹

¹ *Institute of Astronomy, Madingley Rd, Cambridge CB3 0HA*

² *Theoretical Physics, Department of Physics, 1 Keble Road, Oxford, OX1 3NP*

ABSTRACT

This paper introduces a new two-parameter family of dwarf spheroidal (dSph) galaxy models. The mass distribution has a Plummer profile and falls like R^{-4} in projection in agreement with the star-count data. The first free parameter controls the velocity anisotropy, the second controls the dark matter content. The dark matter distribution can be varied from one extreme of mass-follows-light through a near-isothermal halo with flat rotation curve to the other extreme of an extended dark halo with harmonic core. This family of models is explored analytically in some detail – the distribution functions, the intrinsic moments and the projected moments are all calculated.

For the nearby Galactic dSphs, samples of hundreds of discrete radial velocities are becoming available. A technique is developed to extract the anisotropy and dark matter content from such data sets by maximising the likelihood function of the sample of radial velocities. This is constructed from the distribution function and corrected for observational errors and the effects of binaries. Tests on simulated data sets show that samples of ~ 1000 discrete radial velocities are ample to break the degeneracy between mass and anisotropy in the nearby dSphs. Interesting constraints can already be placed on the distribution of the dark matter with samples of ~ 160 radial velocities (the size of the present-day data set for Draco).

The *Space Interferometry Mission* or SIM allows very accurate differential astrometry at faint magnitudes. This can be used to measure the internal proper motions of stars in the nearby Galactic dSphs. Our simulations show that ~ 100 proper motions are sufficient to demolish completely the mass-anisotropy degeneracy. The target stars in Draco are at magnitudes of $V \sim 19 - 20$ and the required proper motion accuracy is $3 - 6 \mu\text{as yr}^{-1}$. The measurement of the proper motions of a sample of ~ 100 stars uncontaminated with binaries will take about 400 hours of SIM time, or under 2% of the mission lifetime.

Key words: galaxies: individual: Draco, Sculptor – galaxies: kinematics and dynamics – Local Group – dark matter – celestial mechanics, stellar dynamics

1 INTRODUCTION

The dark matter content of low-luminosity dwarf galaxies, as inferred from analyses of their internal stellar and gas kinematics, makes them the most dark matter dominated of all galaxies (Mateo 1998, Carignan & Beaulieu 1989). Of these small galaxies, the low-luminosity gas-free dwarf spheroidals (dSph) are the most extreme. Available stellar kinematic studies provide strong evidence for the presence of dominant dark matter (e.g., Aaronson 1983, Mateo 1998), confirming speculations based on estimates of the dSph’s tidal radii (Faber & Lin 1983). Although there have been alternative suggestions as to the origin of the large mass-to-light ratios of the dSphs (e.g., Kuhn & Miller 1989, Kroupa 1997), none of these have carried much conviction – see, for example, the objections raised by Sellwood & Pryor (1997) and Mateo (1997). The spatial distribution of the dark matter in the dSphs is very poorly known. Three obvious possibilities suggest themselves. First, the dark matter may shadow

the stars and so the mass distribution may follow the light. Second, the dark matter may be distributed in a halo which generates a flat rotation curve, as is the case for galaxies like the Milky Way or M31. Third, the scale length of the dark matter may be larger than the luminous matter and so the dSph may lie in the harmonic core of an extended dark matter halo. One promising way to distinguish between these is by dynamical modelling.

Amongst the nearest dSphs are Draco and Sculptor, at heliocentric distances of 82 and 79 kpc, respectively. Both are very attractive candidates for the study of dark matter through dynamical modelling being relatively simple systems with evidence for substantial dark matter content. The Draco dSph has an inferred central mass-to-light ratio of ~ 60 in solar V-band units, while Sculptor has a less extreme value of ~ 10 (Mateo 1998). Any robust dynamical analysis is eased if the potential is approximately steady-state, and if the tracer stellar distribution is in equilibrium and well-mixed. The internal crossing times of the dSphs are

typically only

$$t_{\text{cross}} \sim R/\sigma \sim 2 \times 10^7 (R/200 \text{ pc})(10 \text{ kms}^{-1}/\sigma) \text{ yr.} \quad (1)$$

The Draco dSph is dominated by an intermediate-age to old stellar population, but with little star formation for the last ~ 5 Gyr (Hernandez, Gilmore & Valls-Gabaud 2000). Deep HST imaging of a small field in the outer regions of the Sculptor dSph has revealed a stellar population that is old and metal-poor, similar to halo globular clusters, with little spread in age (Monkiewicz et al. 1999) or metallicity (Mateo 1998). Thus, star formation indeed ceased many crossing times ago and both these systems should be well-mixed. Radial velocity surveys are available for both Draco (Hargreaves et al. 1996; Armandroff et al. 1995) and Sculptor (Queloz, Dubath & Pasquini 1995). Sculptor is of particular current interest due to the detection of significant amounts of HI gas projected within its tidal radius, at a consistent velocity to be truly associated with the dSph (Carignan et al. 1998).

The aim of this paper is to provide new models for the dSphs and new techniques for probing the dark matter distribution. Section 2 describes our models and their intrinsic properties, while Section 3 presents the observable properties, including the distributions of radial velocities. In Section 4, Monte Carlo simulations are used to assess how radial velocity surveys and proper motions inferred from astrometric satellites discriminate between different dark matter distributions. There are already samples of over a hundred radial velocities available for Draco, and this will rise to several hundreds in the next few years. The *Space Interferometry Mission* (SIM, see “<http://sim.jpl.nasa.gov/>”) has the capabilities to measure the internal proper motions of stars in Draco. We assess the likely impact of the new data sets and devise strategies for exploiting them. Finally, a companion paper in this issue of *Monthly Notices* presents an application of the models and algorithm to a newly acquired data set for Draco (Kleyna et al. 2001, henceforth Paper II)

2 DWARF SPHEROIDAL MODELS

2.1 Potential and Density

In the past, dSphs have often been fitted using isotropic, spherical, single component King (1962) models (e.g., Hodge 1966). These are flexible and convenient, but they do come at the cost of very strong assumptions – namely that mass follows light and that all the stars have a Maxwellian distribution of velocities out to the tidal radius. Anisotropic King models relax the latter assumption, but still assume that the distributions of mass and light are identical. Representation of the dark matter and stars as two components of a multi-mass King model is not physically appropriate as such models assume energy equipartition among the different mass classes, which is certainly not the case in a collisionless system such as a dSph. Noting this caveat, Pryor and Kormendy (1990) applied such a model to data on the light distributions and central velocity dispersions of the Draco and Ursa Minor dSphs and found that models in which the luminous and dark matter had similar distributions were favoured over models with more extended dark matter distributions. However, the assumed coupling

between the dark and luminous matter means that changing the velocity anisotropy of these models affects the distribution of the luminous matter. In this paper, instead, we build a family of fully consistent distribution functions for the stars in a dSph, where we assume that the stars are tracer particles, moving in the underlying dark matter potential. This allows us to probe the mass-anisotropy degeneracy discussed above.

Plummer’s (1911) model was originally developed to fit the light distribution of the globular clusters, but a much better application is to fit the light distribution of the dSphs (Lake 1990). For example, Figure 1 shows the best fitting Plummer profile as compared to the background-subtracted star count data of two Galactic dSphs, Draco and Sculptor, as given in Irwin & Hatzidimitriou (1995). With the exception of the Sagittarius and Ursa Minor dSphs, all the remaining seven Galactic dSphs are roughly spherical, with ellipticities lying between 0.13 (Leo II) and 0.35 (Sextans). So, the assumption of spherical symmetry is reasonable. We envisage our models as being particularly useful for Draco and Sculptor, because they are nearby and a wealth of kinematical data is either already available or will become so over the next few years.

Accordingly, let us take the luminosity density of the dSph as

$$\rho(r) = \frac{\rho_0}{[1 + (r/r_0)^2]^{5/2}}, \quad (2)$$

where ρ_0 is determined by the total observed luminosity. The surface brightness of the dSph is

$$\Sigma(R) = \frac{4}{3} \frac{\rho_0 r_0}{[1 + (R/r_0)^2]^2}, \quad (3)$$

where R is the projected radius. The physical meaning of r_0 is that it is the radius of the cylinder that contains half the light; henceforth r_0 is set to unity.

Our aims are to assess the severity of the degeneracy between velocity anisotropy and mass in the dSphs and to investigate what radial velocity surveys may teach us. We need a flexible family of dSph models with differing dark matter distributions and velocity anisotropies, but fitting the same star count profiles on the sky. So, we assume that the potential of the system has the form

$$\psi(r) = \begin{cases} \frac{\psi_0}{[1 + r^2]^{\alpha/2}} & \text{if } \alpha \neq 0, \\ -\frac{v_0^2}{2} \log [1 + r^2] & \text{if } \alpha = 0, \end{cases} \quad (4)$$

where $-2 \leq \alpha \leq 1$. Setting $\psi_0 = v_0^2/\alpha$, the circular velocity curve is

$$v_{\text{circ}}^2 = v_0^2 \frac{r^2}{[1 + r^2]^{1+\alpha/2}}. \quad (5)$$

In other words, the circular velocity curve falls off asymptotically like $r^{-\alpha/2}$. This dark matter potential nicely spans the range of dark matter density distributions which we wish to probe: $\alpha = 1$ corresponds to a mass-follows-light Plummer potential and a Keplerian fall-off at large radii; $\alpha = 0$ yields an asymptotically flat rotation curve; and $\alpha = -2$ gives a harmonic oscillator potential corresponding to the central regions of an extended dark-matter halo. Note that, as the parameter α decreases, the dSph becomes more and more

Table 1. The numerical constants in the DFs. These are pure numbers fixed once and for all by the choice of the anisotropy parameter γ and the dark matter parameter α .

$\alpha > 0$	$L^2 \leq 2E$	$C_{\alpha,\gamma} = \frac{\rho_0}{\psi_0^{5/\alpha-\gamma/\alpha}} \frac{\Gamma(5/\alpha - \gamma/\alpha + 1)}{(2\pi)^{3/2} \Gamma(5/\alpha - \gamma/\alpha - 1/2)}$
$\alpha > 0$	$L^2 \geq 2E$	$C_{\alpha,\gamma} = \frac{\rho_0}{\psi_0^{5/\alpha-\gamma/\alpha}} \frac{\Gamma(5/\alpha - \gamma/\alpha + 1)}{(2\pi)^{3/2} \Gamma(1 - \gamma/2) \Gamma(5/\alpha + \gamma/2 - \gamma/\alpha - 1/2)}$
$\alpha = 0$	$\forall L^2, E$	$C_{0,\gamma} = \frac{\rho_0}{v_0^3} \left(\frac{(5-\gamma)}{2\pi} \right)^{3/2}$
$\alpha < 0$	$L^2 \leq 2E$	$C_{\alpha,\gamma} = \frac{\rho_0}{(-\psi_0)^{5/\alpha-\gamma/\alpha}} \frac{\Gamma(\gamma/\alpha - 5/\alpha + 3/2)}{(2\pi)^{3/2} \Gamma(\gamma/\alpha - 5/\alpha)}$
$\alpha < 0$	$L^2 \geq 2E$	$C_{\alpha,\gamma} = \frac{\rho_0}{(-\psi_0)^{5/\alpha-\gamma/\alpha}} \frac{\Gamma(\gamma/\alpha - 5/\alpha - \gamma/2 + 3/2)}{(2\pi)^{3/2} \Gamma(1 - \gamma/2) \Gamma(\gamma/\alpha - 5/\alpha)}$

dark matter dominated.

Figure 2 shows the variation of the central and average mass-to-light ratio as a function of the model parameters α (which controls the amount of dark matter present) and ν (which measures the anisotropy of the velocity distribution – see section 2.3). It is important to bear in mind that these mass-to-light ratios correspond to models with the same star count density and the same central velocity dispersion. The figure provides a telling indication of the severity of the degeneracy between anisotropy and mass, since the mass-to-light ratio varies by an order of magnitude as we scan the models. It is this degeneracy we wish to break with kinematic measurements.

2.2 Distribution Functions

We now build the distributions of velocities that supports the dSph stellar density (2) in the dark matter potential (4). As is well known, once the velocity distribution is permitted to be anisotropic, there are many possible ways of building a given density from stellar orbits (see Binney & Tremaine 1987, chap. 4). The even part of the distribution function (DF) is determined by the stellar density law, the odd part by the stellar streaming or rotation law. There is no evidence for rotation in the Draco or Sculptor dSphs, so we calculate only the even part of the DF.

2.2.1 Isotropic DFs

According to Jeans’ (1915) theorem, the DF of the stars in a potential is a function entirely of the isolating integrals of motion. Isotropic models have DFs that depend only on the binding energy E . The isotropic DFs are found from Eddington’s (1916) inversion formula as:

$$F(E) = \begin{cases} C_{\alpha,0} |E|^{5/\alpha-3/2} & \text{if } \alpha \neq 0, \\ C_{0,0} \exp(5E/v_0^2) & \text{if } \alpha = 0, \end{cases} \quad (6)$$

where the numerical constants $C_{\alpha,0}$ are given in Table 1. These are very simple results – compare, for example, the much more complicated isotropic DFs of the spherical isochrone (written out in Binney & Tremaine 1987) or the Hernquist (1990) sphere. The only other spherical models with comparably simple DFs are the power-law spheres (Evans 1993, 1994).

2.2.2 Anisotropic DFs: $\alpha > 0$

Anisotropic DFs of spherical models depend on both the energy E and the norm of the angular momentum L . The DFs contain an additional parameter γ , which we shall see shortly controls the anisotropy. We begin by writing the Plummer density (2) in terms of the spherical polar radius r and the potential $\psi(r)$. There are many ways to do this, and each one corresponds to a different anisotropic DF. We choose the density partition

$$\rho = \rho_0 \left(\frac{\psi}{\psi_0} \right)^{5/\alpha-\gamma/\alpha} (1+r^2)^{-\gamma/2}. \quad (7)$$

For the case of a falling rotation curve ($\alpha > 0$), we can exploit the results in Appendix A to obtain the DF as

$$F(E, L^2) = C_{\alpha,\gamma} |E|^{(5-\gamma)/\alpha-3/2} H(E, L^2). \quad (8)$$

When $L^2 \leq 2|E|$, then

$$H(E, L^2) = {}_2F_1 \left(\frac{\gamma}{2}, \frac{3}{2} + \frac{\gamma-5}{\alpha}, 1; \frac{L^2}{2E} \right), \quad (9)$$

whereas when $L^2 \geq 2|E|$, then

$$H(E, L^2) = \left| \frac{2E}{L^2} \right|^{\frac{\gamma}{2}} {}_2F_1 \left(\frac{\gamma}{2}, \frac{\gamma}{2}, \frac{\gamma-1}{2} + \frac{5-\gamma}{\alpha}; \frac{2E}{L^2} \right). \quad (10)$$

Here, ${}_2F_1$ is the hypergeometric function of Gauss, while the numerical constants $C_{\alpha,\gamma}$ are given in Table 1. This result generalises an earlier calculation by Dejonghe (1987), which is restricted to the case where mass follows light ($\alpha = 1$). Note that (10) is not the analytic continuation of (9) beyond the unit circle $\frac{L^2}{2E} = 1$.

It is worth remarking that when $\gamma = -2n$, the hypergeometric function reduces to a polynomial of order n in $\frac{L^2}{2E}$, and then the DFs (8) are entirely elementary. For example, when $\gamma = -2$, we obtain

$$F(E, L^2) = C_{\alpha,-2} |E|^{7/\alpha-3/2} \left[1 - \left(\frac{3}{2} - \frac{\gamma}{\alpha} \right) \frac{L^2}{2|E|} \right]. \quad (11)$$

2.2.3 Anisotropic DFs: $\alpha < 0$

For the case of a rising rotation curve ($\alpha < 0$), we use the density partition

$$\rho = \rho_0 \left(\frac{-\psi}{-\psi_0} \right)^{5/\alpha-\gamma/\alpha} (1+r^2)^{-\gamma/2}. \quad (12)$$

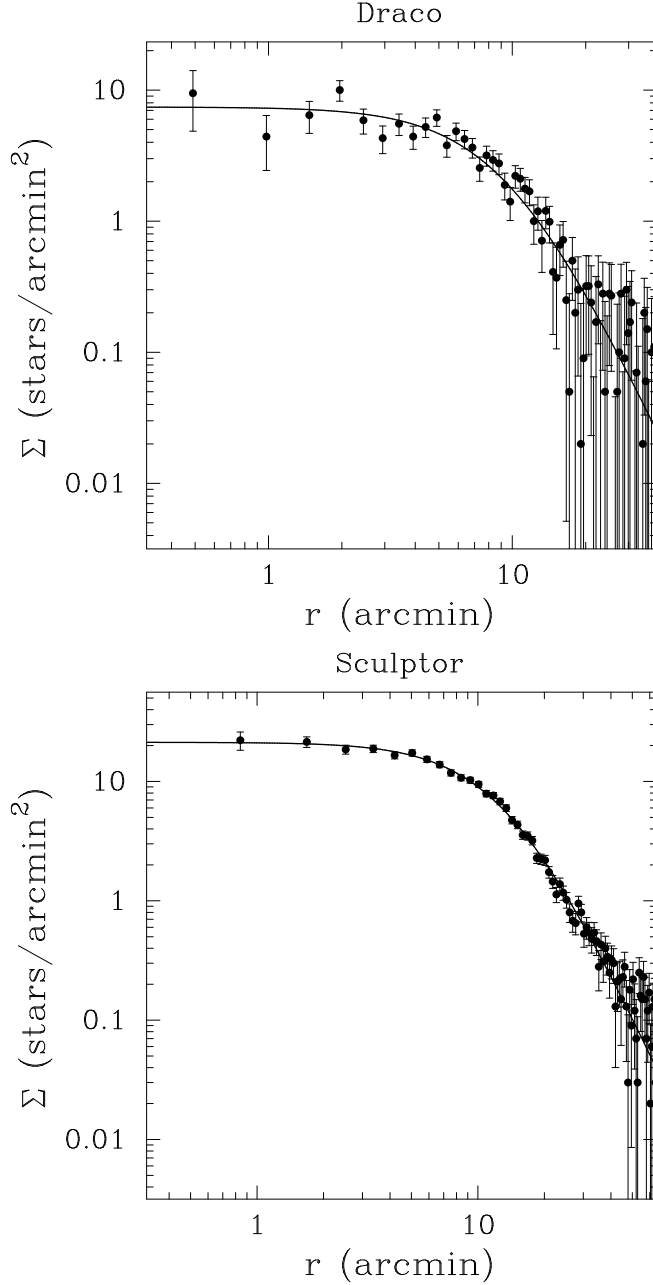


Figure 1. This shows the projected density of the best fitting Plummer model for Draco (upper panel) and Sculptor (lower panel). The data are the background-subtracted star count major axis profiles given by Irwin & Hatzidimitriou (1995). ($r_0 = 9.71$ arcmin for Draco and 13.64 arcmin for Sculptor).

We develop the necessary formula for the anisotropic DF corresponding to this partition in Appendix A. The result is

$$F(E, L^2) = C_{\alpha, \gamma} |E|^{(5-\gamma)/\alpha-3/2} G(E, L^2). \quad (13)$$

When $L^2 \leq 2|E|$, the function $G(E, L^2)$ takes the form;

$$G(E, L^2) = {}_2F_1\left(\frac{\gamma}{2}, \frac{3}{2} + \frac{\gamma-5}{\alpha}, 1; \frac{L^2}{2E}\right), \quad (14)$$

whereas when $L^2 \geq 2|E|$, we have;

$$\begin{aligned} G(E, L^2) &= \left| \frac{2E}{L^2} \right|^{\frac{\gamma}{2}} {}_2F_1\left(\frac{\gamma}{2}, \frac{\gamma}{2}, \frac{\gamma-1}{2} + \frac{5-\gamma}{\alpha}; \frac{2E}{L^2}\right) + \left| \frac{2E}{L^2} \right|^{\frac{3}{2} + \frac{\gamma-5}{\alpha}} \\ &\times \frac{\Gamma(\frac{3}{2} + \frac{\gamma-5}{\alpha}) \Gamma(\frac{\gamma}{2} - \frac{3}{2} + \frac{5-\gamma}{\alpha}) \Gamma(1 - \frac{\gamma}{2})}{\Gamma(\frac{\gamma}{2}) \Gamma(\frac{5-\gamma}{\alpha} - \frac{1}{2}) \Gamma(\frac{3}{2} + \frac{\gamma-5}{\alpha} - \frac{\gamma}{2})} \\ &\times {}_2F_1\left(\frac{3}{2} + \frac{\gamma-5}{\alpha}, \frac{3}{2} + \frac{\gamma-5}{\alpha}, \frac{5-\gamma}{2} + \frac{\gamma-5}{\alpha}; \frac{2E}{L^2}\right) \end{aligned} \quad (15)$$

This time, (15) is the analytic continuation of (14) beyond the unit circle (e.g., eq [15.3.7] of Abramowitz & Stegun

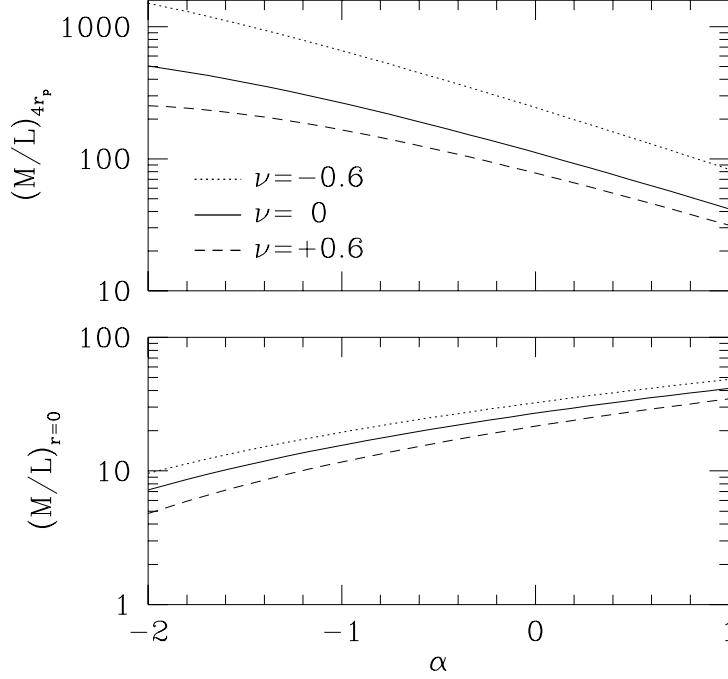


Figure 2. Variation of mass-to-light ratio (in units of M_{\odot}/L_{\odot}) as a function of α for three different ν values. The parameter ν measures the anisotropy of the velocity distribution. Models with $\nu = 0$ are everywhere isotropic, while models with positive (negative) ν become increasingly radial (tangential) at large radii (see section 2.3 for discussion). The top panel shows the total M/L within $4r_0$ ($3r_0 \approx$ Draco King tidal radius; Irwin & Hatzidimitriou 1995). The bottom panel shows the central M/L .

1970).

Again, it is worth remarking that when $\gamma = -2n$, the expression reduces to a polynomial of order n in $\frac{L^2}{2E}$, and then the DFs (13) are entirely elementary. For example, when $\gamma = -2$, we obtain

$$F(E, L^2) = C_{\alpha, -2} |E|^{7/\alpha - 3/2} \left[1 - \left(\frac{3}{2} - \frac{7}{\alpha} \right) \frac{L^2}{2|E|} \right], \quad (16)$$

which is the same as above (11).

2.2.4 Anisotropic DFs: $\alpha = 0$

The case of a flat rotation curve ($\alpha = 0$) has a different form again. We write the Plummer density as

$$\rho = \rho_0 \exp\left(\frac{(5 - \gamma)\psi}{v_0^2}\right) (1 + r^2)^{-\gamma/2}. \quad (17)$$

The DF corresponding to this density partition is derived in Appendix A. We find:

$$F(E, L^2) = C_{0, \gamma} \exp\left(\frac{(5 - \gamma)E}{v_0^2}\right) \Phi\left(\frac{\gamma}{2}, 1, \frac{(\gamma - 5)L^2}{2v_0^2}\right), \quad (18)$$

where Φ denotes the degenerate hypergeometric function and the constant $C_{0, \gamma}$ is given in Table 1. When $\gamma = -2n$, the function Φ reduces to the Laguerre polynomial L_n (see eq. [8.972.1] of Gradshteyn & Ryzhik 1978):

$$F(E, L^2) = \rho_0 \left(\frac{2n + 5}{2\pi v_0^2}\right)^{\frac{3}{2}} L_n \left[\frac{-(2n + 5)L^2}{2v_0^2} \right] \times \exp\left(\frac{(2n + 5)E}{v_0^2}\right). \quad (19)$$

The DFs (18) are then entirely composed of elementary functions, namely the product of a polynomial of the angular momentum and the exponential of the energy. It is worth writing out the lowest member to emphasise its simplicity. When $\gamma = -2$, we have:

$$F(E, L^2) = \rho_0 \left(\frac{7}{2\pi v_0^2}\right)^{\frac{3}{2}} \left[1 + \frac{7L^2}{2v_0^2} \right] \exp\left(\frac{7E}{v_0^2}\right). \quad (20)$$

2.2.5 Practical Evaluation of the DFs

The DFs (8), (13) and (18) all depend on the hypergeometric function in one way or another. Numerical evaluation of the hypergeometric function can be difficult. In fact, none of the algorithms for evaluating the hypergeometric function ${}_2F_1(a, b, c; z)$ presented in the standard reference books on numerical methods (e.g., Press et al. 1992) is applicable for all values of the parameters a, b and c . This is because very different strategies are required depending on the magnitude and signs of the parameters. Our computational algorithm is presented in Appendix B. Note that in our applications to calculations of the likelihoods in Section 4, it is important that the DFs are calculated extremely accurately. The obvious way of checking our numerical algorithm is to investigate whether the integration of the DF over velocity space yields the Plummer density. Typically, we find that the density is recovered to better than one part in 10^6 .

2.3 Intrinsic Moments

Although the DFs (8), (13) and (18) have differing forms according to whether the rotation curve is falling ($\alpha > 0$), flat ($\alpha = 0$) or rising ($\alpha < 0$), nonetheless all physical quantities like the moments vary smoothly and continuously with the rotation curve index α .

The intrinsic velocity second moments are

$$\langle v_r^2 \rangle = \frac{v_0^2}{(\alpha+5-\gamma)} \frac{1}{(1+r^2)^{\alpha/2}}, \quad (21)$$

$$\langle v_\theta^2 \rangle = \langle v_\phi^2 \rangle = \frac{v_0^2}{(\alpha+5-\gamma)} \frac{1}{(1+r^2)^{\alpha/2}} \left[1 - \frac{\gamma}{2} \frac{r^2}{1+r^2} \right]. \quad (22)$$

The second moments converge and are positive definite provided $\gamma < \min(\alpha+5, 2)$.

In terms of Binney's (1981) anisotropy parameter α , the radial and tangential velocity dispersion $\langle v_r^2 \rangle$ and $\langle v_\theta^2 \rangle$ vary as

$$\beta = 1 - \frac{\langle v_\theta^2 \rangle}{\langle v_r^2 \rangle} = \frac{\gamma}{2} \frac{r^2}{1+r^2}. \quad (23)$$

If $\gamma = 0$, the velocity dispersions are isotropic. Irrespective of γ , the central regions of the model are always isotropic. At large radii, the anisotropy becomes constant (c.f., Hénon 1973; Wilkinson & Evans 1999). If $\gamma < 0$, then the dispersion tensor becomes tangential with increasing radius; if $\gamma > 0$, it becomes radial. The limit $\gamma \rightarrow -\infty$ is the circular orbit model, while the limit $\gamma \rightarrow 2$ is built from radial orbits alone in the outer parts.

It is also helpful to define the quantity ν which is related to γ by

$$\nu = \log_{10} \left(\frac{2}{2-\gamma} \right)$$

This quantity runs from $-\infty$ (tangential velocity distribution at large radii) to $+\infty$ (radial velocity distribution at large radii). The velocity distribution is everywhere isotropic for $\nu = 0$. This definition is helpful because the ranges of tangential and radial anisotropy are symmetric about $\nu = 0$.

The intrinsic fourth moments are useful for diagnosing deviations from pure Gaussianity and so we briefly list the results here:

$$\langle v_r^4 \rangle = \frac{v_0^4}{(\alpha+5-\gamma)(2\alpha+5-\gamma)} \frac{1}{(1+r^2)^\alpha}, \quad (24)$$

$$\langle v_r^2 v_\theta^2 \rangle = \langle v_r^2 v_\phi^2 \rangle = \frac{v_0^4}{(\alpha+5-\gamma)(2\alpha+5-\gamma)} \frac{1}{(1+r^2)^\alpha} \times \left[1 - \frac{\gamma}{2} \frac{r^2}{1+r^2} \right], \quad (25)$$

$$\langle v_\theta^4 \rangle = \langle v_\phi^4 \rangle = \frac{v_0^4}{8(\alpha+5-\gamma)(2\alpha+5-\gamma)} \frac{1}{(1+r^2)^\alpha} \times \left[(4-\gamma)(2-\gamma) + \frac{2\gamma(2-\gamma)}{1+r^2} + \frac{\gamma(2+\gamma)}{(1+r^2)^2} \right]. \quad (26)$$

All the remaining components of this fourth rank tensor vanish. The fourth moments converge and are positive definite provided $\gamma < \min(2\alpha+5, 2)$.

3 OBSERVABLE PROPERTIES

The properties of dSphs when viewed in projection are of particular interest to us, since these correspond to observable quantities. In this section, we present the distributions of the line of sight velocities and the proper motions. All the moments of these distributions are analytic.

3.1 Line of Sight Moments

To derive the line of sight velocity moments involves performing a triple integration along the line of sight and over the two velocity components perpendicular to the line of sight. For our dSph models, these integrals are all analytic. The line of sight second moment is given by

$$\sigma_P^2(R) = \frac{\sigma_0^2}{(1+R^2)^{\alpha/2}} \left[1 - \frac{\gamma(4+\alpha)}{2(5+\alpha)} \frac{R^2}{1+R^2} \right] \quad (27)$$

where the central velocity dispersion is

$$\sigma_0^2 = \frac{3\sqrt{\pi}v_0^2\Gamma(2+\alpha/2)}{4(\alpha+5-\gamma)\Gamma(5/2+\alpha/2)}. \quad (28)$$

When $\alpha = 1$, this reduces to the result found by Dejonghe (1987) for his self-consistent Plummer models. The left panels of Figure 3 show the variation of the line of sight second moment with projected radius R for $\alpha = -1, 0, 1$ and $\gamma = 2, 0, -10$ (or, equivalently, $\nu = \infty, 0, -0.8$). For $\alpha > 0$ and $\gamma \leq -\alpha(5+\alpha)/(4+\alpha)$, the curves $\sigma_P(R)$ show a maximum at

$$R^2 = \frac{2(\alpha(5+\alpha) + \gamma(4+\alpha))}{\alpha(\gamma(4+\alpha) - 2(5+\alpha))}. \quad (29)$$

As Figure 3 indicates, the models have an unusual and attractive feature. For a given α , all the curves pass through the same point

$$R^2 = \frac{2}{2+\alpha}, \quad \sigma_P^2 = \frac{3\sqrt{\pi}v_0^2}{8} \frac{\Gamma(2+\alpha/2)}{\Gamma(7/2+\alpha/2)} \left(\frac{2+\alpha}{4+\alpha} \right)^{\alpha/2}, \quad (30)$$

irrespective of γ . This radius is the *changeover radius*. Radially anisotropic dSphs ($\gamma, \nu > 0$) have less projected velocity dispersion σ_P at large radii than isotropic dSphs, and more σ_P at small radii. This follows from simple geometrical considerations. Radial orbits contribute significantly to the line of sight motion in the inner parts, but much less so in the outer parts. Conversely, tangentially anisotropic dSphs ($\gamma, \nu < 0$) have more projected velocity dispersion σ_P at large radii than isotropic dSphs, and less σ_P at small radii. The changeover radius is the radius at which the transition from the central to the asymptotic properties occurs.

The line of sight fourth moment is useful for detecting deviations from Gaussianity. It can be calculated from the intrinsic fourth moments as:

$$\sigma_P^4(R) = \frac{\sigma_0^4}{(1+R^2)^\alpha} \left[1 - \frac{2\gamma(2+\alpha)}{(5+2\alpha)} \frac{R^2}{1+R^2} + \frac{\gamma(2+\gamma)(2+\alpha)(3+\alpha)}{2(5+2\alpha)(7+2\alpha)} \frac{R^4}{(1+R^2)^2} \right], \quad (31)$$

with the central value given by

$$\sigma_0^4 = \frac{9\sqrt{\pi}v_0^4\Gamma(\alpha+2)}{4(\alpha+5-\gamma)(2\alpha+5-\gamma)\Gamma(5/2+\alpha)}. \quad (32)$$

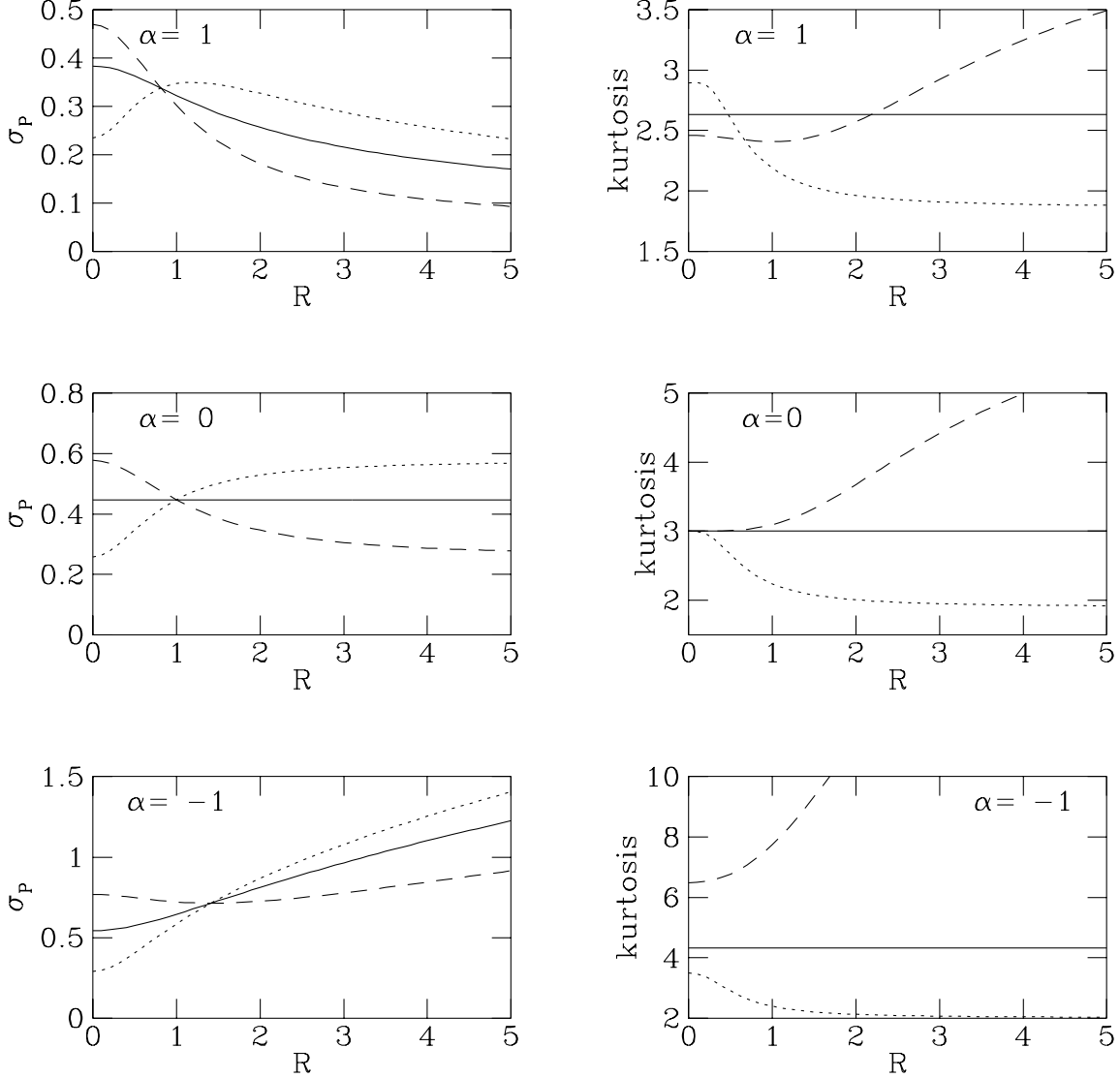


Figure 3. This shows the variation of the line of sight second moments (left panels) and kurtosis (right panels) with radius R on the plane of the sky for models with different dark matter content ($\alpha = 1, 0, -1$ as labelled). The full curves refer to the isotropic model ($\nu = 0$), the dashed curve to a radially anisotropic model ($\nu = \infty$), the dotted curves to a tangentially anisotropic model ($\nu = -0.8$).

In fact, all the line of sight moments are analytic. The n th moment σ_p^{2n} is

$$\sigma_p^{2n}(R) = \frac{\sigma_0^{2n}}{(1+R^2)^{n\alpha/2}} {}_3F_2\left(-n, \frac{\gamma}{2}, \frac{4+n\alpha}{2}; 1, \frac{5+n\alpha}{2}; \frac{R^2}{1+R^2}\right), \quad (33)$$

where ${}_3F_2$ is the generalised hypergeometric function (which always reduces to a finite n th order polynomial). The central value is

$$\sigma_0^{2n} = 2^{n-2} \frac{3\psi_0^n \Gamma(n+1/2) \Gamma(5/\alpha - \gamma/\alpha + 1) \Gamma(2+n\alpha/2)}{\Gamma(5/\alpha - \gamma/\alpha + n + 1) \Gamma(5/2 + n\alpha/2)}. \quad (34)$$

Figure 3 shows the variation of the kurtosis $\kappa = \sigma_p^4 / (\sigma_p^2)^2$ with projected radius R . The kurtosis measures

the extent to which the distribution is peaked. A Gaussian distribution has a kurtosis of 3. The larger the kurtosis, the broader is the distribution. The isotropic models ($\gamma, \nu = 0$) always have a constant kurtosis given by

$$\kappa = \frac{4}{\sqrt{\pi}} \frac{\Gamma(\alpha+2) \Gamma(\alpha/2+5/2) \Gamma(\alpha/2+7/2)}{\Gamma(\alpha+7/2) \Gamma^2(\alpha/2+2)}. \quad (35)$$

In fact, the $\alpha = \gamma, \nu = 0$ model has a constant kurtosis of 3, indicating that the line profiles of this model are Gaussian. Figure 3 illustrates the tendency for increasing kurtosis as the dSph becomes more dark matter dominated. This stems predominantly from the larger tails in the intrinsic velocity distributions. As α diminishes, there are more and more high

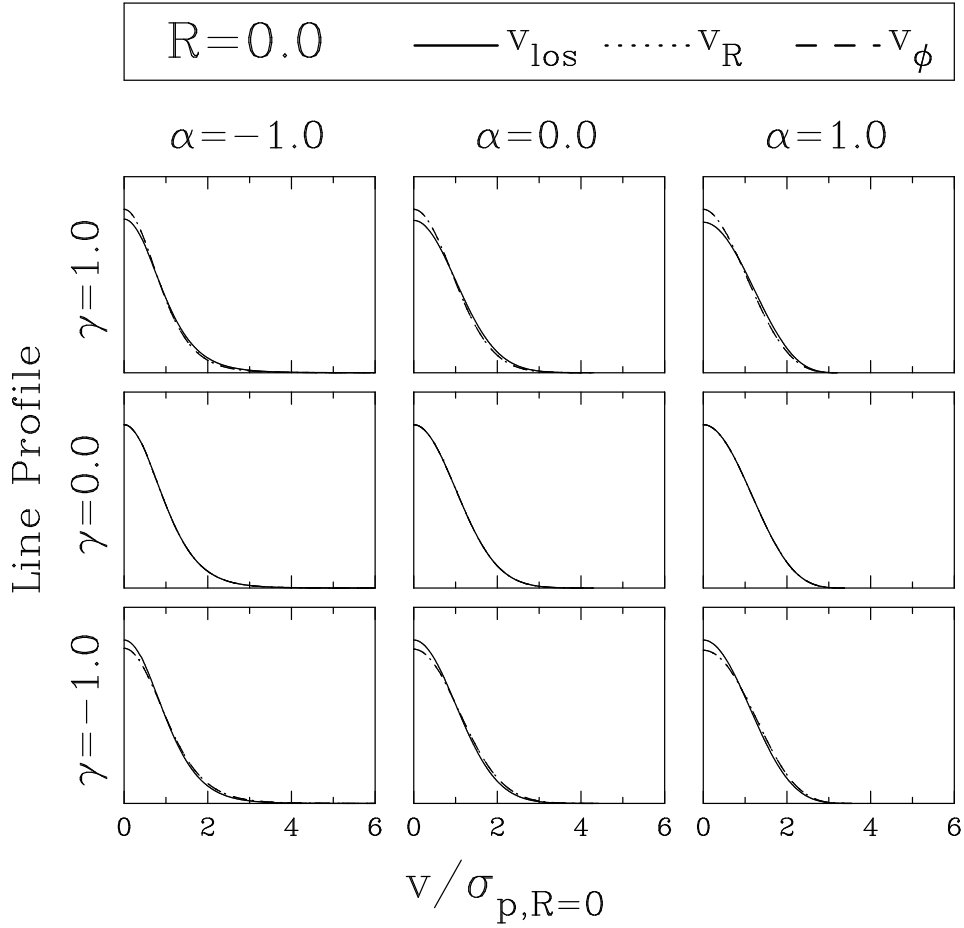


Figure 4. Normalised line profiles or distributions of line of sight velocities v_{los} are shown for models with different dark matter content ($\alpha = 1, 0, -1$ as labelled) and different anisotropy ($\nu = -0.6, 0, 0.6$). The line profile is calculated at $R = 0$, the center of the dSph in projection. For comparison, the distributions of proper motions (v_R and v_ϕ) on the plane of the sky are also shown – these profiles are identical for $R = 0$ and appear superposed as a dot-dashed line.

velocity stars in the tails.

3.2 The Line Profiles

When comparing models to the discrete radial velocities, the main quantity of interest is the line profile. This is the probability distribution of the line of sight velocities at a given projected radius. Mathematically, the unnormalised line profile $L(v_{\text{los}}, R)$ is the integral of the DF along the line of sight and over the tangential components of velocity. Let us use (R, φ) as polar coordinates on the plane of the sky and z as the coordinate along the line of sight.

When $\alpha \leq 0$, the line profile is:

$$L(v_{\text{los}}, R) = \int_{-\infty}^{\infty} dz \int_{-\infty}^{\infty} dv_R \int_{-\infty}^{\infty} dv_\varphi F(E, L^2), \quad (36)$$

whereas when $\alpha > 0$, the line profile is:

$$L(v_{\text{los}}, R) = \int_{z_-}^{z_+} dz \int_{-(2\psi - v_{\text{los}}^2)^{1/2}}^{(2\psi - v_{\text{los}}^2)^{1/2}} dv_R \times \int_{-(2\psi - v_{\text{los}}^2 - v_R^2)^{1/2}}^{(2\psi - v_{\text{los}}^2 - v_R^2)^{1/2}} dv_\varphi F(E, L^2). \quad (37)$$

If $\alpha \leq 0$, then the integration over the line of sight extends indefinitely. If $\alpha > 0$, the stars with velocities v_{los} are seen at projected position R only if $v_{\text{los}}^2 < 2\psi(R, z)$. This provides upper and lower limits z_\pm to the line of sight integral. Often it is useful to divide by the surface brightness $\Sigma(R)$ and consider normalised line profiles $\ell(v_{\text{los}}, R) = L(v_{\text{los}}, R)/\Sigma(R)$.

For the isotropic models, the line profiles can be reduced easily to single quadratures. When $\alpha \neq 0$, the unnormalised line profiles have the form

$$L(v_{\text{los}}, R) = \sqrt{\frac{2}{\pi}} \frac{K_\alpha \rho_0}{|\psi_0|^{5/\alpha}} \times \int_R^\infty \left| \psi(r) - \frac{1}{2}v_{\text{los}}^2 \right|^{5/\alpha - 1/2} \frac{r dr}{\sqrt{r^2 - R^2}}. \quad (38)$$

where

$$K_\alpha \begin{cases} \frac{\Gamma(5/\alpha + 1)}{\Gamma(5/\alpha + 1/2)} & \text{if } \alpha < 0, \\ \frac{\Gamma(1/2 - 5/\alpha)}{\Gamma(-5/\alpha)} & \text{if } \alpha > 0. \end{cases} \quad (39)$$

If and only if the rotation curve is flat ($\alpha = 0$) and the model is isotropic ($\gamma, \nu = 0$), then the normalised line profile is a

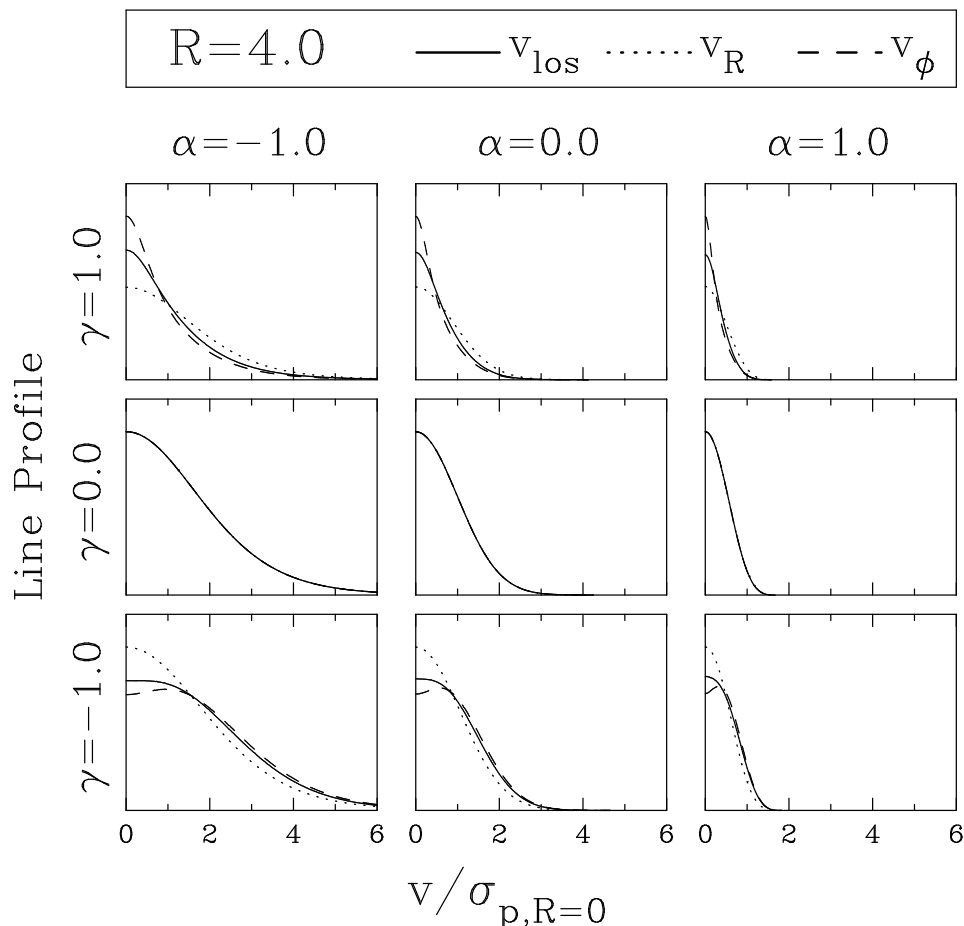


Figure 5. As Figure 4, but for locations at projected position $R = 4$.

pure Gaussian

$$\ell(v_{\text{los}}, R) = \left(\frac{5}{2\pi v_0^2}\right)^{1/2} \exp\left(-\frac{5v_{\text{los}}^2}{2v_0^2}\right). \quad (40)$$

We emphasise that the line profiles vary smoothly and continuously through the seemingly singular case of $\alpha = 0$. This may be verified by taking the limit $\alpha \rightarrow 0$ of (38).

Although presently unmeasurable with ground-based telescopes, the internal proper motions of stars in the nearby dSphs are accessible to future space missions (like the *Space Interferometry Mission* or SIM). In Draco and Sculptor, the stars of interest are at magnitudes $V \sim 19 - 20$ and the required proper motion accuracy corresponding to $1 - 2 \text{ km s}^{-1}$ in velocity is $3 - 6 \mu\text{as yr}^{-1}$, which is just within the capabilities of SIM. Hence, it is also useful to calculate the one dimensional distributions of proper motions $L(v_R, R)$ or $L(v_\varphi, R)$ by integrating along the line of sight and over the other two transverse velocities.

Figures 4 and 5 present some examples of line profiles and proper motion distributions obtained for a variety of values of R , α and γ . These are calculated by direct integration over the DFs. For the isotropic models ($\gamma, \nu = 0$), the line profile and the proper motion distributions clearly coincide. Tangentially anisotropic clusters tend to show bimodal line profiles, whereas radially anisotropic clusters tend to have narrower, peaked line profiles. Hence, the trend as we move

vertically downwards in the panels is towards broader and more flat-topped profiles. The larger the dark matter content, the greater and more distended the wings of the line profiles. So, the trend as we move left to right in the panels is towards less extended line profiles.

Note that, as we move outwards from the center of the dSph, the differences between the line profiles become more pronounced. Observationally speaking, it is easier to obtain radial velocities for stars in the centre, but it is stars in the outer parts of the dSph which are most useful for breaking the degeneracy between mass and anisotropy.

4 METHODOLOGY

Previous studies of dSph dynamics have been impeded by the degeneracy between anisotropy and mass. An increase in the line of sight velocity dispersion at large radii may be due to either (1) the presence of large amounts of mass at large radii, or (2) tangential anisotropy in the velocity distribution. The large observed central radial velocity dispersion is compatible with either a massive halo, and a low central density; or no halo, and a large central density. In this section, we test our ability to discern between these possibilities using (i) large radial velocity surveys and (ii) radial velocities and proper motions provided by SIM.

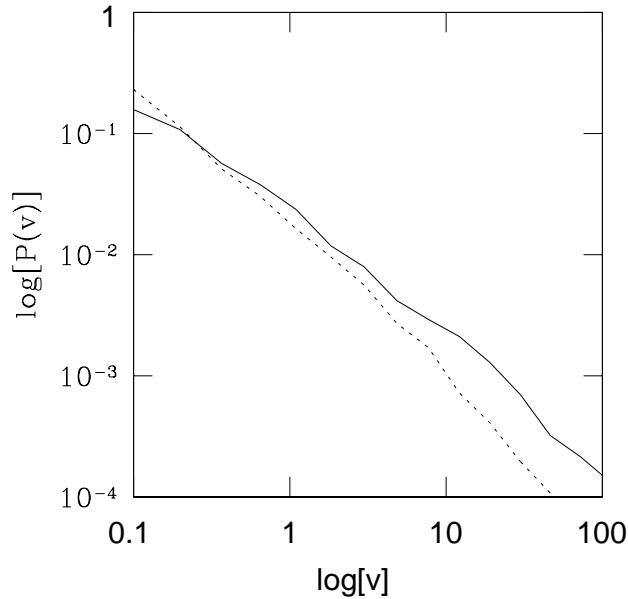


Figure 6. Distribution of binary velocities as inferred from the binary distribution in the solar neighbourhood. Dashed curve – un-evolved distribution. Solid curve – evolved distribution for giant star binaries. See text for details.

4.1 The Likelihood Function

The problem of comparing discrete radial velocity measurements to galactic models has already received much attention (e.g., Little & Tremaine 1987, Kochanek 1996, Wilkinson & Evans 1999, Evans & Wilkinson 2000). Suppose we are given radial velocities $v_{\text{los}i}$ (corrected for the galaxy mean velocity) of N stars in a dSph at projected positions R_i . At each point, we can compute the probability of observing the radial velocity data set

$$P(\{R_i, v_{\text{los}i}\}_{i=1\dots N} | \alpha, \gamma) = \prod_{i=1}^N \ell(R_i, v_{\text{los}i}; \alpha, \gamma). \quad (41)$$

So, we scan a grid of α, γ , and at each point compute the probability of observing the entire input data set. Using Bayes' theorem and assuming uniform prior probabilities in the model parameters, then the most likely values of α and γ are given by maximising (41). Confidence regions are obtained by applying two-dimensional χ^2 statistics to the likelihood (or the logarithm of (41)).

This procedure requires repeated evaluation of the line profiles, and direct integration over the DF is too slow and expensive to provide a competitive algorithm. Accordingly, we only use brute force integration to provide a look-up table of the line profiles in a grid in the four-dimensional (α, γ, R, v) space. The grid spacing in α, R and v is linear, whereas the spacing in γ is uniform in $\log(2-\gamma)$. We use cubic splines to interpolate in the logarithm of the line profile between the grid points. Once the look-up table has been built, this provides an extremely fast and accurate way of calculating the line profiles. Typically, the error in the line profile (as inferred by integration over the line of sight velocity to recover the surface density) is better than one part in 10^3 . This is still sufficient to mislead our maximum likelihood algorithm because the probability (41) is formed by

the multiplication of N line profiles. To take account of this small error, we re-normalise each line profile to unity after interpolation.

Before applying the likelihood algorithm, there are two further corrections that must be applied. First, the line profile is convolved with a Gaussian of width 2 km s^{-1} to allow for observational errors. This is a typical error for data obtained on the 4m class telescopes like the William Herschel Telescope with multi-object spectrographs. Second, the line profile is adjusted for the effect of binaries. This also involves convolution, this time with the binary correction function $b(v)$. By Monte Carlo sampling binary orbits drawn from the binary distribution in the solar neighbourhood, taking account of tidal circularisation of the orbits as described in Paper II, we deduce the distribution of velocities $P_b(v)$ induced by the binary motion. This is shown in Figure 6. The binary correction function is then given by

$$b(v) = f P_b(v) + (1 - f) \delta(v), \quad (42)$$

where the constant f is the binary fraction.

4.2 Radial Velocity Surveys

Synthetic data sets are created by choosing phase space coordinates $\{R_i, z_i, v_{Ri}, v_{\varphi i}, v_{\text{los}i}\}_{i=1\dots N}$ drawn from the DF, and then discarding all but the projected positions and the line of sight velocities. The velocities are contaminated by measurement noise of amplitude 2 km s^{-1} , and a fraction f of the stars are also assigned a binary velocity which is added to their line of sight velocity. To reduce the computation time, rather than randomly selecting the projected radius for each star, ten values of the projected radius R_i between 0.0 and 2.5 are used. Each data set is then analysed and a most likely value of α and γ (or, equivalently, ν) is obtained.

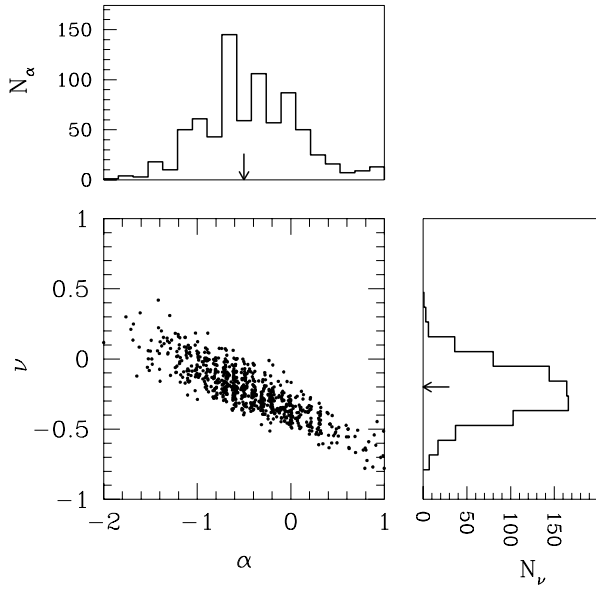


Figure 7. The recovery of the dark matter parameter α and the anisotropy ν from simulated data sets of 160 radial velocities. Observational errors of 2 km s^{-1} are assumed for the radial velocities and a binary fraction of 40% is assumed. The main panel shows where each data set falls in the (α, ν) plane. The side panels show the one-dimensional histograms. The true values of α and ν are marked with arrows.

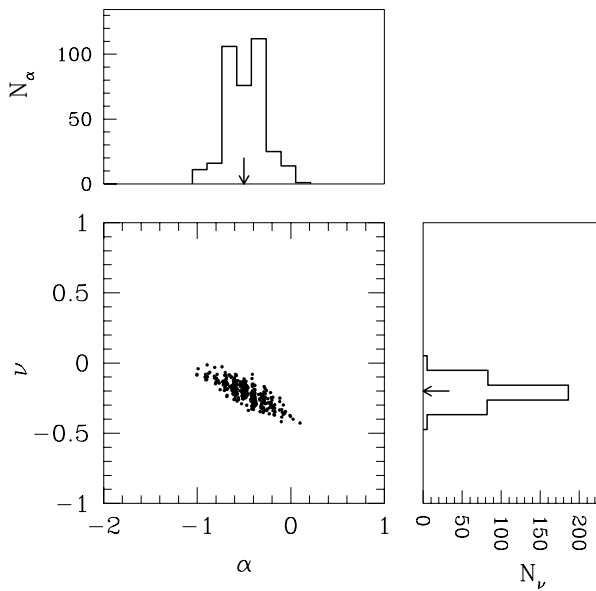


Figure 8. As Figure 7, but for simulated data sets of 1000 radial velocities each.

Figure 7 shows the results from the analysis of simulated data sets of 160 radial velocities. This is the number of radial velocities that are presently available for Draco. Figure 8 shows the results from analysis of simulated data sets of 1000 radial velocities. This is an estimate of the maximum number of radial velocities that may be available in Draco with an

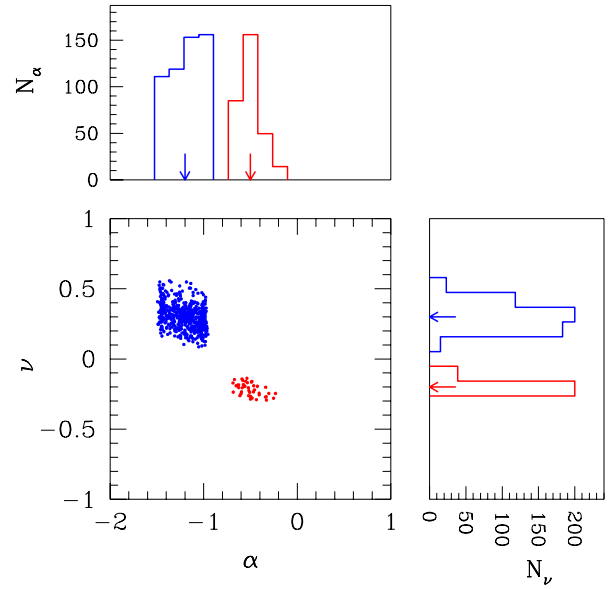


Figure 9. The recovery of the dark matter parameter α and the anisotropy ν for simulated data sets of 160 stars with ground-based radial velocities, together with proper motions measured by SIM. The true values of α and ν are marked with arrows.

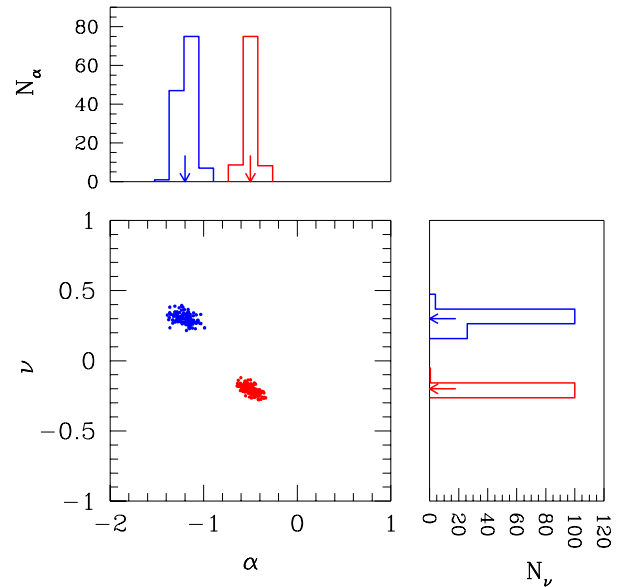


Figure 10. As Figure 9, but for simulated data sets of 1000 stars with radial velocities and proper motions.

observing program on a 4m class telescope. In each figure, the scatter plot shows the joint distribution of α and ν values obtained from the artificial data sets while the histograms show the spread in the individual parameter values.

Even with a data set of the present size, Figure 7 shows that it is possible to put interesting constraints on the value of α . The input model for Figure 7 had an α value of -0.5 indicating a dark matter distribution intermediate between that of a flat rotation curve halo and an extended harmonic

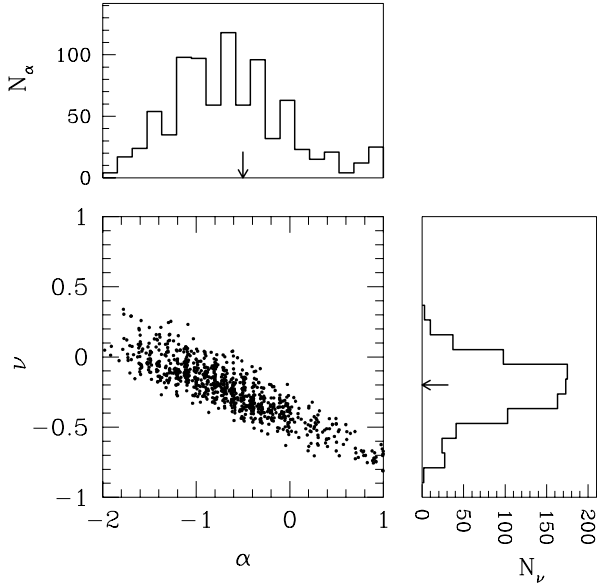


Figure 11. The recovery of the dark matter parameter α and the anisotropy ν for simulated data sets of 160 stars with radial velocities. Data produced with a binary fraction of 80% but analysed assuming a binary fraction of 40%.

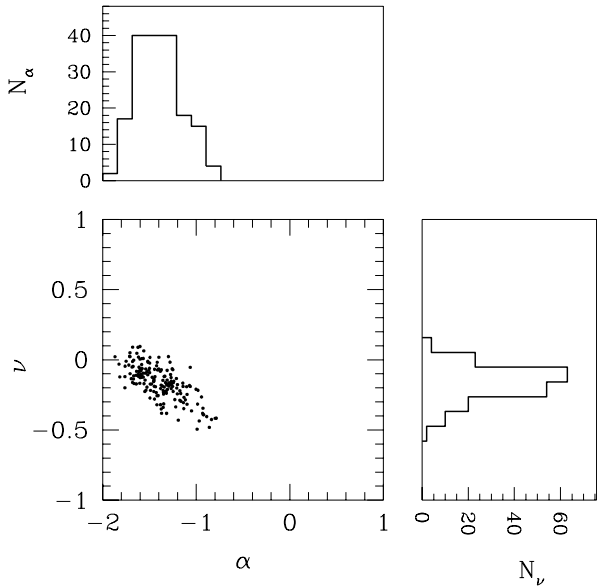


Figure 12. The recovery of the dark matter parameter α and the anisotropy ν for simulated data sets of 160 stars with radial velocities. Data generated from a model with a Jaffe sphere representing the dark halo of the dSph. See text for details.

core. From the figure, the 2σ confidence interval on α is $(-1.45, 0.8)$. Thus data sets containing 160 radial velocities are sufficient to rule out a mass-follows-light halo model ($\alpha = 1$) at about the 2.5σ level. Increasing the size of the data set to 1000 stars allows much greater discrimination between models.

4.3 Proper Motion Surveys

Here, we consider the possible impact of next generation astrometric satellites like SIM and its successors. Microarc-second astrometry to an accuracy $3 - 6 \mu\text{as yr}^{-1}$ is sufficient to allow the internal proper motions of the brightest stars in Draco to be measured to $1 - 2 \text{ km s}^{-1}$. Since all stars in Draco are at almost the same distance, only the relative proper motions are required and this significantly reduces the observing time. A further advantage is that all the target stars are within a $\sim 1^\circ$ field of view, allowing subdivision of the observations into a small number of overlapping fields and hence reducing the instrumental systematic contribution to the error. A satellite like SIM is ideal for these measurements, as it allows very accurate differential measurements at faint magnitudes.

To simulate this, we pick phase space coordinates $\{x_i, y_i, v_{x_i}, v_{y_i}, v_{z_i}\}_{i=1\dots N}$ drawn from the DF, discard the geocentric radial position coordinate z , and attempt to recover α and ν using the Bayesian likelihood. As in the radial velocity simulations described above, we contaminate the data with measurement noise in each component of velocity. The correct expression for the probabilities required to analyse these data is then the 3-dimensional convolution of the DF with 3 Gaussians, each of width 2 km s^{-1} . However, as was noted earlier, integration of the DF is computationally expensive, and we therefore approximate the convolution by a weighted sum over the values of the DF at the corners of a cube of side $\sqrt{2}\sigma$. This approach gives sufficiently accurate results for the present paper – in the future, increases in computational speed will allow us to perform the full 3-dimensional convolution. At present, we consider only the case where no binaries are present. This is both computationally convenient, and may be justified on the basis that proper motion measurements will be based on multiple epoch observations which will allow the identification of binaries in our sample.

Figure 9 shows the results from the analysis of simulated data sets of 160 with both radial velocities and proper motions measured for each star to an accuracy of 2 km s^{-1} . Figure 10 shows the results from analysis of similar data sets containing 1000 stars. The narrow spread visible in these histograms, particularly in the case of 1000 stars, emphasises the value of having all components of the stellar velocities when modelling the mass profile. The key feature of these results, as illustrated in Figure 9, is that even with only 160 proper motions it is possible to break unambiguously the degeneracy between mass and anisotropy.

4.4 Robustness

In this section, we consider the robustness of our analysis to errors in the estimation of the sample binary fraction and measurement errors. As the same algorithm is used in both cases, we present results only for the former case. We also address the question of the extent to which our analysis is model dependent.

Let us begin by considering data sets in which the binary fraction has been severely underestimated. Data sets of 160 radial velocities are generated as described earlier, assuming a binary fraction of 80%, and measurement errors of 2 km s^{-1} . However, when analysing the data, we perform

the convolution of the line profiles assuming a binary fraction of only 40%. This discrepancy represents an upper limit to the uncertainty in the binary fraction in a typical data set of single-epoch radial velocities. The results of this experiment are shown in Figure 11. Comparison of this figure with Figure 7 shows that while the distributions of recovered α and γ values are slightly broadened, the overall effect of the mis-estimation of the binary fraction is not serious. The uncertainty caused by the true size of observational errors can be checked in a similar manner. We generate data sets of 160 radial velocities with a binary fraction of 40% and measurement errors of 4 km s^{-1} . However, we convolve the line profiles with an error Gaussian of width 2 km s^{-1} representing an over-optimistic estimation of the measurement errors. We do not show a figure for this case, as the results are predictable. Our algorithm is not confused and the results are clustered around the correct values, albeit with a greater spread.

A more serious question is whether our maximum likelihood algorithm – which assumes a parametrised fit for the density and potential – is robust, as any dSph undoubtedly deviates to a greater or lesser extent from the model. To test this, we generate synthetic data from a very different halo model and analyse them using our models. We retain the assumption that the light in the dwarf follows a Plummer profile, but we replace the halo with a Jaffe (1983) sphere. The halo potential is then given by

$$\psi(r) = v_c^2 \log \left(\frac{r + r_J}{r} \right)$$

where v_c is the amplitude of the halo rotation curve at small radii, and r_J is the scale radius of the halo. For these simulations, we set $r_J = 1$ and $v_c = 45.5 \text{ km s}^{-1}$, yielding a halo whose rotation curve falls off for $r > 1$ but for which total mass enclosed within $r \sim 3$ is similar to that of an $\alpha \sim -2$ (rising rotation curve) model from our family of Plummer halo models. Following Wilkinson & Evans (1999, Eq. (19)) we build a DF (with constant velocity anisotropy β) of the form $F(E, L) = L^{-2\beta} f(E)$. The value of β is set to be the mean value of the velocity anisotropy between $r = 0$ and $r = 3$ for a model with $\nu = -0.2$ from our Plummer family. We analyse the data using radial velocities alone.

Figure 12 shows the results obtained from data sets of 160 radial velocities. The analysis of the Jaffe model data sets returns Plummer model parameter values in the region of $\alpha = -1.5$, $\nu = -0.2$. Qualitatively, this result is very encouraging, as the parameter estimates all lie in the region of the (α, γ) plane where the dark matter is more extended than the light in the dSph. More quantitatively, the Jaffe data sets return approximately the correct value of ν . The mass enclosed within $r = 3$, the region probed by the generated data points, is also recovered to better than a factor of two – for the (input) Jaffe model we obtain $3.6 \times 10^8 M_\odot$, while for the recovered Plummer halo we obtain $2.2 \times 10^8 M_\odot$. We conclude that the parameter values returned by our method are reasonably robust, even for a small data set, and that they do reflect underlying physical properties of the data.

5 CONCLUSIONS

This paper has presented a flexible family of spherical models suitable for representing dwarf spheroidal (dSph) galax-

ies. The models have a Plummer profile, which is an excellent fit to the star count data on the nearby dSphs. There are two free parameters. The first is the dark matter parameter α . When $\alpha = 1$, the mass follows the light and the rotation curve is asymptotically Keplerian; when $\alpha = 0$, the dark matter is distributed in a cored isothermal sphere and the rotation curve is flat; when $\alpha = -1$, the dSph is enclosed within the harmonic core of a much larger dark matter halo. The second parameter is the anisotropy parameter γ . When $\gamma > 0$, the models are radially anisotropic at large radii; when $\gamma = 0$, they are isotropic; when $\gamma < 0$, they are tangentially anisotropic at large radii.

These models offer considerable advantages over King models, which are conventionally used for fitting dSphs (see e.g. Binney & Tremaine 1987). The single component, isotropic King models often used for modelling the dSphs assume that the mass follows the light and have an isotropic stellar velocity distribution. The cost of such strong assumptions is that they are unable to probe the degeneracy that exists between dark matter mass and anisotropy. A very attractive property of our new models is that the intrinsic and projected moments are simple and analytic. In particular, the line of sight velocity dispersion is available as a function of projected radius for all values of the dark matter and anisotropy parameters. The phase space distribution function (DF) is more complicated – as it depends on transcendental functions – but it is feasible to evaluate numerically. Quadratures over the DF provide us with the distributions of radial velocities (the line profiles) as well as the distributions of proper motions. All these observable quantities are readily available for our family of dSph models! Note that the line profiles of all the models are similar in the centre, but begin to differ at $\sim 2r_0$, emphasising the importance of gathering data at large radii.

We have used our new models to assess what large samples of radial velocities can tell us about dark matter in dSphs. All of the information on the kinematics is contained in the DF. So, given large samples of stars with projected positions and radial velocities, we calculate the likelihood of observing the data set as a function of the dark matter and anisotropy parameters. The distribution of radial velocities is corrected first for observational errors by convolution with a Gaussian and second for the contamination by binaries by convolution with a suitable correction function.

Simulated data sets of 160 and 1000 radial velocities are drawn from the DF, contaminated with measurement noise and binary velocities, and fed into the likelihood algorithm. A sample size of hundreds of velocities is typical of the presently available data sets, whereas a sample size of a thousand velocities is an estimate of the number that may be accessible to a long-term observing program in the nearby dSphs like Draco. Our simulations show that a sample size of 160 stars is already sufficient to make interesting statements about the dark matter distribution in a dwarf galaxy. In particular, using data drawn from a model with a slightly rising rotation curve it is possible to rule out mass-follows-light models at about the 2.5σ confidence level. Larger radial velocity data sets allow much tighter constraints to be placed on the model parameters. Our machinery is set to work in a companion paper (Kleyna et al. 2001) to interpret a newly acquired data set for the Draco dSph.

The addition of proper motion data completely breaks

the degeneracy between mass and velocity anisotropy, even using only a hundred or so proper motions. Obtaining such a data set will be feasible using the SIM satellite. One strategy is to construct a sample of stars that are uncontaminated by binaries before SIM flies, for example, by taking second and third epoch data on ground-based telescopes and removing all radial velocity variables. SIM time is very expensive and it is wasteful to spend it following the astrometric paths of binaries if our aim is to measure the proper motions of single stars. In Draco and Sculptor, the target stars are at magnitudes $V \sim 19$ and the required proper motion accuracy corresponding to $1 - 2 \text{ km s}^{-1}$ in velocity is $15 - 30 \mu\text{as}$ over the mission lifetime of 5 years. The optimum strategy is to measure the positions of the stars twice, once at the beginning and once at the end of the mission. This will be ample to calculate the proper motions, provided all binaries have been eliminated by our ongoing radial velocity surveys. SIM takes ~ 1 hour to measure the position of $V \sim 19$ star to $\sim 20 \mu\text{as}$ (in one dimension), which is our typical required accuracy. Hence, for each star, we require 4 hours of SIM time (for two-dimensional measurements at the beginning and end of the mission). Our simulations have shown that samples of ~ 100 proper motions are ample to break the mass-anisotropy degeneracy. This will take about 400 hours of SIM time, or roughly 1.7% of the mission lifetime. In other words, *this is an extremely competitive use of SIM time.*

Given the modest amount of SIM time required, our collaboration is considering an ambitious program that acquires the proper motions of roughly a hundred stars in each of Draco, Ursa Minor and Sextans. This program will still only consume 5% of the mission lifetime. Such a data set, together with the sophisticated modelling techniques we have introduced in this paper, will make it possible to map the dark matter distribution in these three dSph galaxies with unprecedented accuracy. This important test of the nature of dark matter on such small scales is uniquely possible with SIM.

ACKNOWLEDGMENTS

MIW and JK acknowledge financial support from PPARC. NWE thanks the Royal Society for financial support and Andy Gould for a number of insightful remarks about the Space Interferometry Mission.

REFERENCES

- Aaronson M., 1983, ApJ, 266, L11
Abramowitz M., Stegun I.A., 1970, Handbook of Mathematical Functions (Dover: New York)
Armandroff T.E., Olszewski E.W., Pryor C. 1995, AJ, 110, 2131
Binney J., 1981, MNRAS, 196, 455
Binney J., Tremaine S. 1987, Galactic Dynamics, (Princeton University Press, Princeton)
Carignan C., Beaulieu S. 1989, ApJ, 347, 760
Carignan C., Beaulieu S., Côté S., Demers S., Mateo M. 1998, AJ, 116, 1690
Dejonghe H. 1986, Phys. Rept., 133, Nos. 3-4, 225
Dejonghe H. 1987, MNRAS, 224, 13
Eddington A.S. 1916, MNRAS, 76, 572
Evans N.W. 1993, MNRAS, 260, 191
Evans N.W. 1994, MNRAS, 267, 333
Evans N.W., Wilkinson M.I. 2000, MNRAS, 316, 929
Faber S.M., Lin D.N.C., 1983, ApJ, 266, 21
Fricke W., 1951, Astron. Nachr., 280, 193
Gradshteyn I.S., Ryzhik I.M., 1978, Tables of Integrals, Series and Products, (Academic Press: New York)
Hargreaves J.C., Gilmore G., Irwin M.J., Carter D., 1996, MNRAS, 282, 305
Hénon M., 1973, A&A, 24, 229
Hernandez X., Gilmore G., Valls-Gabaud D. 2000, MNRAS, 317, 831
Hernquist L. 1990, ApJ, 356, 359
Hodge P.W. 1966, AJ, 71, 204
Irwin M., Hatzidimitriou D. 1995, MNRAS, 277, 1354
Jeans J.H. 1915, MNRAS, 76, 70
Jaffe W., 1983, MNRAS, 202, 995
Kochanek C., 1996, ApJ, 457, 228
King I. 1962, AJ, 67, 471
Kleyna J., Wilkinson M.I., Evans N.W., Gilmore G., 2001, MNRAS, astro-ph/0109450
Kroupa P. 1997, New Astronomy, 2, 139
Kuhn J., Miller R.H. 1989, ApJ, 341, L41
Lake G. 1990, MNRAS, 244, 701
Little B., Tremaine S.D., 1987, ApJ, 320, 493
Luke, Y.L., 1977, Algorithms for the Computation of Mathematical Functions, (Academic Press, London)
Mateo M. 1997, in "The Nature of Elliptical Galaxies", ASP Conf. Ser. 116, ed. M. Arnaboldi, G.S. Da Costa, P. Saha (ASP: San Francisco), 259
Mateo M. 1998, ARAA, 36, 435
Monkiewicz J. et al. (the WFPC2 IDT) 1999, PASP, 111, 1392
Plummer H.C. 1911, MNRAS, 71, 460
Press, W.H., Teukolsky, S.A., Vetterling, W.T., Flannery, B.P., 1992, Numerical Recipes in C, (Cambridge University Press, Cambridge)
Queloz D., Dubath P., Pasquini L. 1995, AA, 300, 31
Sellwood J.A., Pryor C. 1997, Highlights of Astronomy, vol 11, ed. J. Andersen (Kluwer, Dordrecht), 638
Wilkinson M.I., Evans N.W. 1999, MNRAS, 310, 645

APPENDIX A: DERIVATION OF THE DISTRIBUTION FUNCTIONS

First, let us summarise Dejonghe's (1986) results, which apply to the models with falling rotation curves ($\alpha > 0$). Let us start with the well-known result (Fricke 1951, Dejonghe 1987, Evans 1994) that the density ρ'

$$\rho' = \psi^p r^{-\beta}, \quad (43)$$

corresponds to the DF

$$f' = \frac{\Gamma(p+1)}{\Gamma(1-\beta/2)(p-1/2+\beta/2)} \frac{L^{-\beta} E^{p+\beta/2-3/2}}{(2\pi)^{3/2} 2^{-\beta/2}}. \quad (44)$$

These are sometimes called Fricke components. From this simple result, we can build up the DF F corresponding to the density

$$\rho = \psi^p \frac{r^{2a}}{(1+r^2)^{a+b}}, \quad (45)$$

by a continuous superposition of the Fricke components. The result is

$$F(E, L^2) = \frac{\Gamma(p+1)E^{p-3/2}}{(2\pi)^{3/2}\Gamma(a+b)} \mathcal{H}(a, b, p - \frac{1}{2}, 1; \frac{L^2}{2E}), \quad (46)$$

where

$$\mathcal{H}(a, b, c, d; x) = \frac{1}{2\pi i} \int_c \frac{\Gamma(a+s)\Gamma(b-s)}{\Gamma(c+s)\Gamma(d-s)} x^{-s} ds. \quad (47)$$

Here, \mathcal{C} is a contour in the complex s plane such that all the poles $-a-n$ are on the left and all the poles $b+n$ are on the right (where n is an integer). Dejonghe (1986) shows how to evaluate this integral. When $x \leq 1$, the contour is completed to the left by adding a large semi-circle at infinity. Only the poles at $s = -a-n$ are enclosed, giving

$$\mathcal{H}(a, b, c, d; x) = \frac{\Gamma(a+b)x^a}{\Gamma(c-a)\Gamma(a+d)} {}_2F_1(a+b, 1+a-c, a+d; x).$$

When $x > 1$, the contour is completed to the right and only the poles at $s = b+n$ contribute to give

$$\mathcal{H}(a, b, c, d; x) = \frac{\Gamma(a+b)x^{-b}}{\Gamma(d-b)\Gamma(b+c)} {}_2F_1(a+b, 1+b-d, b+c; \frac{1}{x}).$$

Second, let us extend this result to the models with rising rotation curves ($\alpha < 0$). In this case, the Fricke components are derived by Evans (1994) as

$$\rho' = \frac{1}{(-\psi)^p} r^{-\beta}, \quad (48)$$

$$f' = \frac{\Gamma(p - \beta/2 + 3/2)}{\Gamma(1 - \beta/2)\Gamma(p)} \frac{L^{-\beta}}{(-E)^{p-\beta/2+3/2} (2\pi)^{3/2} 2^{-\beta/2}}. \quad (49)$$

Again, we seek the DF F corresponding to the density

$$\rho = \frac{1}{(-\psi)^p} \frac{r^{2a}}{(1+r^2)^{a+b}}. \quad (50)$$

This time the result is

$$F(E, L^2) = \frac{1}{(2\pi)^{3/2} \Gamma(p) \Gamma(a+b)} \times \frac{1}{(-E)^{p+3/2}} \mathcal{G}(a, b, p + \frac{3}{2}, 1; \frac{L^2}{2E}), \quad (51)$$

where

$$\mathcal{G}(a, b, c, d; x) = \frac{1}{2\pi i} \int_{\mathcal{C}} \frac{\Gamma(a+s)\Gamma(b-s)\Gamma(c-s)}{\Gamma(d-s)} (-x)^{-s} ds. \quad (52)$$

Here, \mathcal{C} is a contour in the complex s plane such that all the poles $-a-n$ are on the left and all the poles $b+n$ and $c+n$ are on the right (where n is an integer). When $|x| \leq 1$, we obtain

$$\mathcal{G}(a, b, c, d; x) = \frac{\Gamma(a+b)\Gamma(a+c)(-x)^a}{\Gamma(a+d)} {}_2F_1(a+b, a+c, a+d; x).$$

When $|x| > 1$, the contour is completed to the right and there are two infinite sequences of poles at $b+n$ and $c+n$. We therefore obtain a sum of two hypergeometric functions, namely

$$\mathcal{G}(a, b, c, d; x) = \frac{\Gamma(c-b)\Gamma(a+b)}{(-x)^b \Gamma(d-b)} {}_2F_1(a+b, 1+b-d, 1+b-c; \frac{1}{x}) + \frac{\Gamma(b-c)\Gamma(a+c)}{(-x)^c \Gamma(d-c)} {}_2F_1(a+c, 1+c-d, 1+c-b; \frac{1}{x}).$$

The third and final case is that corresponding to a flat rotation curve ($\alpha = 0$). The elementary Fricke components become

$$\rho' = r^{-\beta/2} \exp(p\psi/v_0^2), \quad (53)$$

and

$$f' = \frac{p^{3/2-\beta/2}}{(2\pi)^{3/2} 2^{-\beta/2} \Gamma(1-\beta/2) v_0^{3-\beta/2}} L^{-\beta/2} \exp(pE/v_0^2). \quad (54)$$

This means that the density

$$\rho = \frac{r^{2a}}{(1+r^2)^{a+b}} \exp(p\psi/v_0^2), \quad (55)$$

corresponds to the DF

$$F = \frac{p^{3/2+a}}{(2\pi)^{3/2} 2^a \Gamma(a+1) v_0^{2a+3}} \exp(pE/v_0^2) \Phi(a+b, a+1, -\frac{pL^2}{2v_0^2}), \quad (56)$$

where Φ is the degenerate hypergeometric function.

APPENDIX B: NUMERICAL COMPUTATION OF HYPERGEOMETRIC FUNCTIONS

The hypergeometric function is defined within the unit circle $z < 1$ by the hypergeometric series

$${}_2F_1(a, b; c; z) = 1 + \frac{ab}{c1!} z + \frac{a(a+1)b(b+1)}{c(c+1)2!} z^2 + \dots + \frac{a(a+1)\dots(a+n-1)b(b+1)\dots(b+n-1)}{c(c+1)\dots(c+n-1)n!} z^n + \dots \quad (57)$$

As the coefficients of the series approach 1 as $n \rightarrow \infty$, the series is bounded by a majorizing geometric series, and converges for $|z| < 1$. Outside of the unit circle, an analytic continuation of the hypergeometric series is given by the hypergeometric differential equation

$${}_2F_1'' = \frac{ab {}_2F_1 - [c-(a+b+1)z] {}_2F_1'}{z(1-z)} \quad (58)$$

A second, linearly independent solution to the hypergeometric differential equation is $z^{1-c} {}_2F_1(a-c+1, b-c+1; 2-c; z)$ (provided c is not an integer).

Numerical evaluation of the hypergeometric function can be awkward. In fact, none of the standard reference books on numerical methods (e.g., Press et al. 1992) present completely general algorithms for the computation of the hypergeometric function valid for all parameter values. Luke (1977) has derived several useful Chebyshev and rational polynomial approximations. The coefficients of the hypergeometric series (and its approximations) may reverse sign, so that the final value can depend on the near-cancellation of very large terms, rendering the normal fifteen digit floating point precision of a computer insufficient. The parasitic secondary solution of the differential equation, by virtue of its steep z^{1-c} growth, renders the integration of the differential equation numerically impracticable for $c \ll 0$.

Our algorithm divides the evaluation of the hypergeometric function into two régimes. Provided $c \gtrsim -3$, the hypergeometric differential equation (58) is stable. It is integrated via the standard ordinary differential equation integration methods provided by Press et al (1992). The initial condition for the integration cannot be chosen as ${}_2F_1(a, b, c; z) = 1$ when $z = 0$, as the differential equation (58) is then singular. Accordingly, we start from $z = \epsilon$ and calculate the value of ${}_2F_1(a, b, c; z)$ at this point by direct summation of the hypergeometric series. This is the method of choice for evaluation of the DF when $\alpha > 0$ or when $\alpha < 0$ and $|L^2/(2E)| \leq 1$.

If $c < -3$ (as occurs in the expressions for the DF when $\alpha < 0$ and $|L^2/(2E)| > 1$) and $z > -0.5$, we compute the power series using standard double precision arithmetic, but switch to arbitrary precision arithmetic whenever the terms

of the series exceed 10^6 , ensuring that the final value will be accurate to nine decimal places. Arbitrary precision arithmetic is necessary only for $\alpha \rightarrow 0$, or $c \ll 0$. If $z < -0.5$ then we use the transformation (see eq. [9.131.1] of Gradshteyn & Ryzhik 1978)

$${}_2F_1(a, b; c; z) = (1 - z)^{-a} {}_2F_1(a, c - b; c; z/(z - 1)) \quad (59)$$

to cast z into $z/(z - 1)$, ensuring that the power series converges swiftly for all z of interest.

This paper has been produced using the Royal Astronomical Society/Blackwell Science \TeX macros.